Influence of cold gas spray parameters on the corrosion resistance of Al-Al_2O_3 coatings sprayed on carbon steel

F. S. da Silva[a,b*], N. Cinca[b], S. Dosta[b], I. G. Cano[b], J. M. Guilemany[b], A. V. Benedetti[a]

[a]*São Paulo State University - UNESP, Institute of Chemistry, Rua Prof. Francisco Degni, 55, C.P. 355, 14800-060, Araraquara, SP, Brazil*

[b]*Barcelona University, CPT, Martí I Franqués 1, 08028 Barcelona, Spain*

*Corresponding author

E-mail address: fernandoquimicauems@gmail.com (F. S. da Silva)

Abstract

This work describes the influence of standoff distance (SoD), and gas temperature on the morphology and corrosion resistance of Al-10%Al_2O_3 coatings deposited by cold gas spray (CGS) on carbon steel. The results showed that the standoff distance had little effect on the thickness and microstructure of the coating. However, a 100 °C decrease of the spraying temperature reduced the coating thickness by 300 µm. The use of electrochemical analyses and SEM images showed that all the coatings studied were able to protect the substrate during at least 1300 h of immersion, due to the dense microstructure obtained by CGS.

Keywords: Reinforced coatings, cold gas spray, Al-Al_2O_3, composite.

1. Introduction

The use of composite coatings produced by cold gas spray (CGS) is currently a key area of research. The technique offers the ability to form a coating composed of a soft matrix with hard reinforcement particles, depending on the feedstock, without additional undesirable phases [1-4]. Of particular interest is that CGS has the potential to produce Al-Al_2O_3 coatings, since ductile aluminum powder can be mixed with harder Al_2O_3 ceramic powder to produce a reinforced coating [1,2]. This composite is already used in the automotive, aerospace, and electronics industries, due to its combination of low density and excellent physical and mechanical properties [1,2].

Cold gas sprayed Al-Al_2O_3 coatings have been successfully deposited on a range of substrates [3-6]. Studies have investigated the coating microstructure, Al:Al_2O_3 ratio, wear performance, and corrosion resistance [3,4,6]. Spencer et al. [4] reported that the addition of Al_2O_3 to pure aluminum increased the hardness and the wear resistance of the coating. An increase of the Al_2O_3 content changes the wear mode from adhesive to abrasive. Qiu et al. [7] reported that the tamping effect provided by Al_2O_3 particles decreased the porosity of coatings, increased the hardness, and improved the wear resistance. Reinforcement with these particles avoids plastic deformation of the Al matrix and diminishes the adhesive wear of the material [8,9]. Cong et al. [6] investigated the mechanical properties and corrosion resistance of Al-25%Al_2O_3 coatings on carbon steel substrate. The porosity value was around 1% and the bond strength was 43 MPa. The corrosion of the coating was initiated from crevices and pores formed due to dissolution of the Al matrix at the Al-Al_2O_3 interface. Tao et al. [3] evaluated the microstructure and corrosion resistance of Al-25%Al_2O_3, and Al-50%Al_2O_3 composite coatings sprayed on AZ91D magnesium alloy. The coatings showed a microstructure with low porosity and high adhesion, while the corrosion resistances of the composite coatings were similar to that of a pure Al coating. In our previous work [10], the

performances of an Al coating and a bilayer of Al-10%Al_2O_3/Al deposited on steel were compared. The results showed that for immersion times shorter than 200 h, the composite coatings provided higher corrosion resistance than the Al coating, due to the lower active area of the electrode. However, for t >200 h, the formation of galvanic couples between the Al matrix and the alumina particles caused severe corrosion of the Al matrix surrounding the particles, which decreased the corrosion resistance of the Al-10%Al_2O_3 coating.

Although the tribological behaviors, microstructures, Al-Al_2O_3 ratios, and corrosion resistances of composite coatings have been reported in the literature, few studies have investigated the influence of the spraying parameters on the corrosion resistance during long immersion times (t >1000 h), especially considering the standoff distance and the gas spraying temperature. Considering all these aspects, the aim of the present work was to investigate the influence of standoff distance (SoD) and gas spraying temperature on the coating microstructure and the corrosion resistance during extended immersion (t ≥1300 h) of Al-10%Al_2O_3 coatings deposited by cold gas spray onto carbon steel.

2. Experimental

2.1. Raw materials and substrate

Aluminum (Al ≥99%) and alumina (Al_2O_3 ≥99%) powders supplied by TLS Technik GmbH (Germany) were used as feedstocks. The substrate was a carbon steel alloy with the composition described previously [10]. Flat (5 cm x 2 cm x 0.5 cm) substrates were cleaned with acetone, followed by grit-blasting using alumina corundum (Al_2O_3, 82±12 μm particle size), which resulted in a surface roughness (Ra) of ~4.7 μm, measured as described elsewhere [10].

2.2 Coatings preparation

The coatings were produced in the Thermal Spray Centre, Barcelona, using a Kinetiks 4000 system (Cold Gas Technology GmbH) equipped with a polymeric nozzle (type 33) and capable of reaching 40 bar pressure and 800 °C, with N_2 as the streaming gas. The coatings were sprayed using a powder ratio of 90%Al:10%Al_2O_3, under three different spray conditions (Table 1).

Table 1. Spraying parameters for the CGS composite coatings.

Sample	SoD (cm)	Temperature (°C)
5T4	5	400
15T4	15	400
15T3	15	300

It was decided to study the effects of SoD and temperature, because these parameters have a major influence on the fabrication and microstructure of the CGS coatings [8]. The other spray parameters were kept constant at a traversing velocity of 500 mm/s, step size of 1 mm, and deposition of five layers.

2.3. Morphological and microstructural characterization, and hardness measurements

The particle size distributions of the powders were determined by laser diffraction spectroscopy (LDS). The phase compositions and microstructures of the coatings were investigated by X-ray diffraction (XRD), using a Siemens D5000 instrument. The morphologies and chemical compositions of the powders and coatings were analyzed by scanning electron microscopy (SEM), using a JEOL JSM-5310 microscope coupled to an X-

ray microanalysis (EDS) system. Cross-sectional SEM images (minimum of 10) were analyzed using Image J software to determine the mean thickness value. Optical images were also used to determine the coating porosity (ASTM E2109-01). The hardness measurements of the coatings and substrate were determined cross sections, according to ASTM E384-99. The mean values were obtained from at least 20 indentations performed at a load of 100 gf on the polished cross sections.

2.4. Corrosion measurements

The corrosion tests were carried out in unstirred and aerated 3.5 wt.% NaCl, at 25 °C. A Tait electrochemical cell [11] and a Bio-Logic potentiostat (Model VSP) were used to acquire the electrochemical data. The protection provided by the coatings was investigated by E_{OCP} and EIS measurements during relatively long immersion times of 120 h (for the carbon steel substrate) and ~1300 h (for the coatings). The EIS measurements were performed from 100 kHz to 5 mHz, applying 10 mV (rms) *vs.* E_{OCP}, at 1 h and then every 24 h during the immersion. Electrical equivalent circuit (EEC) fitting (using Z-view® software) was performed for quantitative analysis of the impedance data. Before the fitting procedure, the consistency of the experimental data was checked using the Kramers-Kronig Transform (KKT) [12].

3. Results and discussion

3.1 Powder characterization

The Al_2O_3 powder consisted of particles with angular shapes (Fig. 1a). The powder size distribution presented a mean value of 62 µm, d_{10} of 41 µm, and d_{90} of 116 µm. The Al powder particles were mostly spherical in shape and without pores (Fig. 1b), with mean particle size of 22 µm, d_{10} of 9 µm, and d_{90} of 52 µm. The X-ray diffractograms (Fig. 2) and

EDS analyses (Fig. S1, *SD*) revealed the presence of only the Al and α-Al_2O_3 phases. The Al content in the feedstock powder was ~98 wt.%, according to the EDS analysis (Fig. S1, *SD*). These characterization results confirmed that the feedstock powder had ideal size and morphology for being sprayed by CGS, as previously discussed by Champagne et al. [8] and Zhao et al. [9].

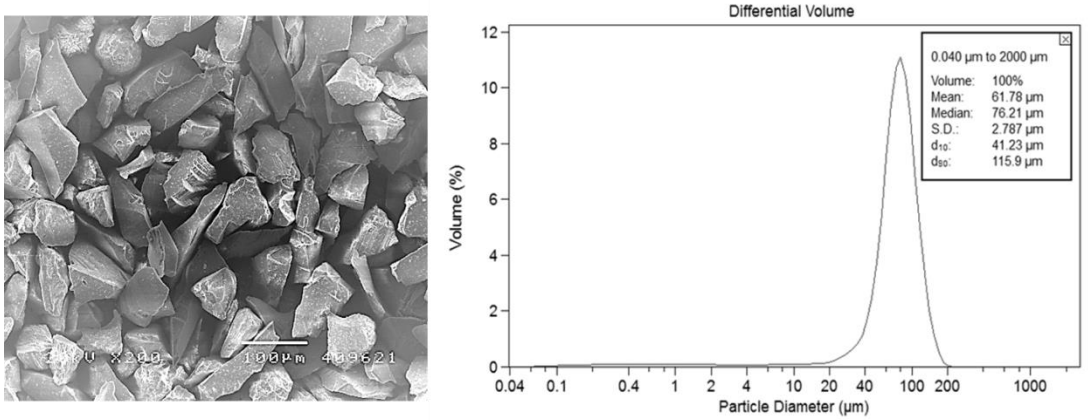

(a)

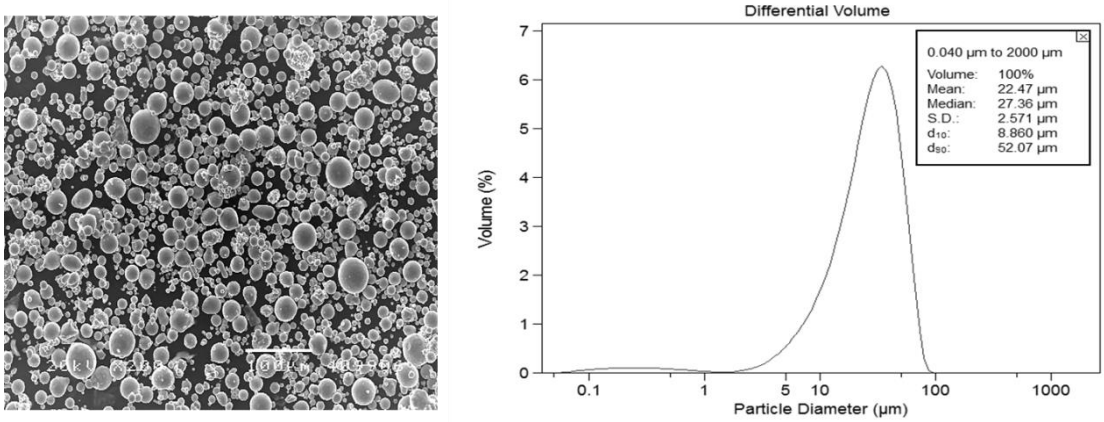

(b)

Fig. 1. SEM images and LDS analyses of the feedstock powders: (a) alumina and (b) aluminum.

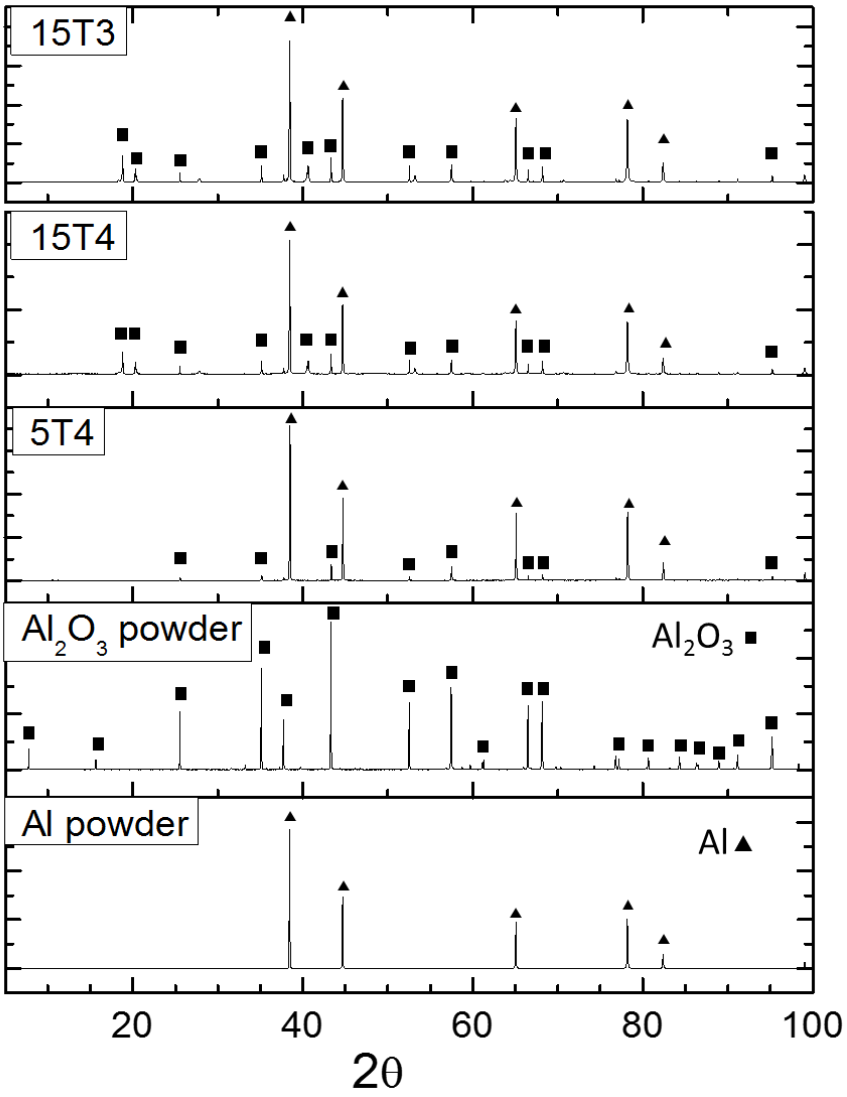

Fig. 2. X-ray diffractograms of the powders and coatings.

3.2 Coatings characterization

The SEM images of the coating cross sections (Fig. 3) revealed a microstructure with some cracks, defects, and pores. For all the coatings, the compactness of the top layer was lower, compared to the bottom layer, as observed previously by Zhou et al. [13]. The coating/substrate interface was free from defects or delamination. The images showed a random distribution of the Al_2O_3 particles, suggesting that under the spray conditions used, the two materials did not separate in the gas flow stream. The Al_2O_3 particles were irregular, with sizes in the range 1-15 μm, which was lower than the size of the starting material, due to

fracture of the particles during collision in the powder jet and the impact with the substrate or previously deposited layers [14,15]. The diffractograms of the coatings and the powder showed the same characteristic peaks (Fig. 2), indicating that the compositions of the feedstock materials and coatings were similar. Since CGS is a solid-state deposition technique, the high kinetic and low thermal energies produce coatings with low oxide contents and without fragile phases [8,16].

The porosity was lower than 0.6%, so the coating could be considered compact. Particles deposited by cold spraying undergo initial deformation on impact, resulting in their adherence to the particles deposited previously, followed by further deformation caused by the impacts of incoming particles, resulting in a tamping effect [3]. In the present case, the high hardness of the Al_2O_3 particles produced much greater deformation in the previously deposited aluminum splats, increasing the tamping effect. This mechanism provides an explanation for the low porosity of the Al-Al_2O_3 coatings.

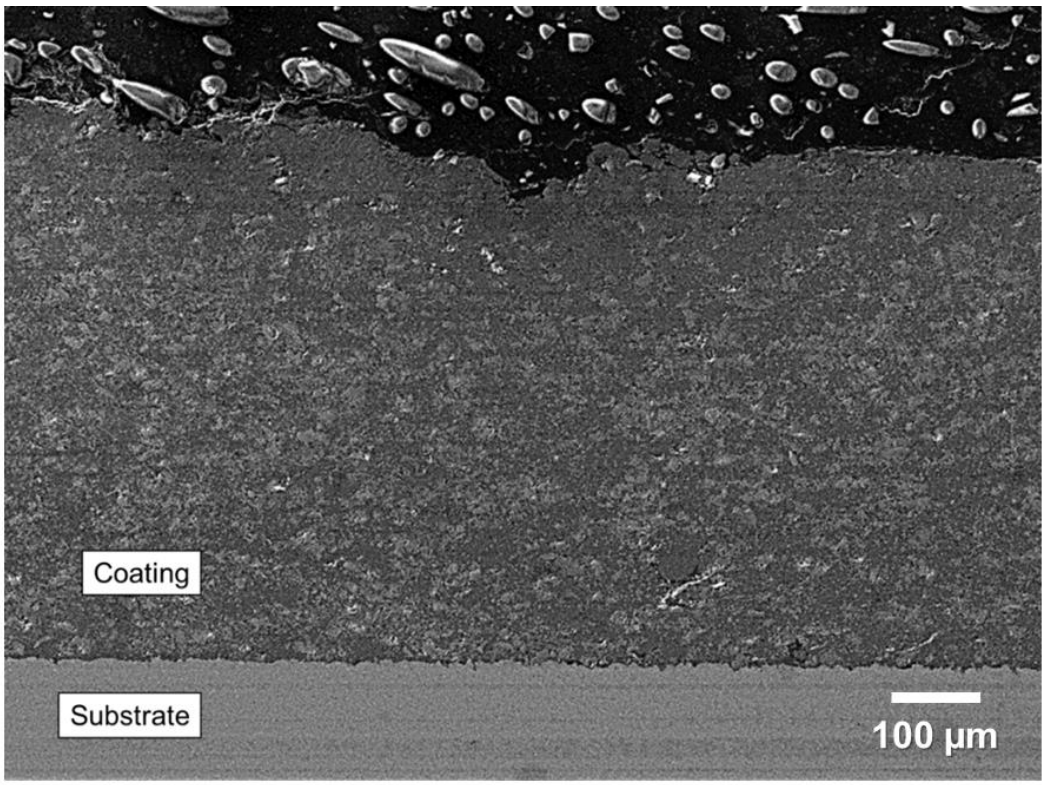

(a)

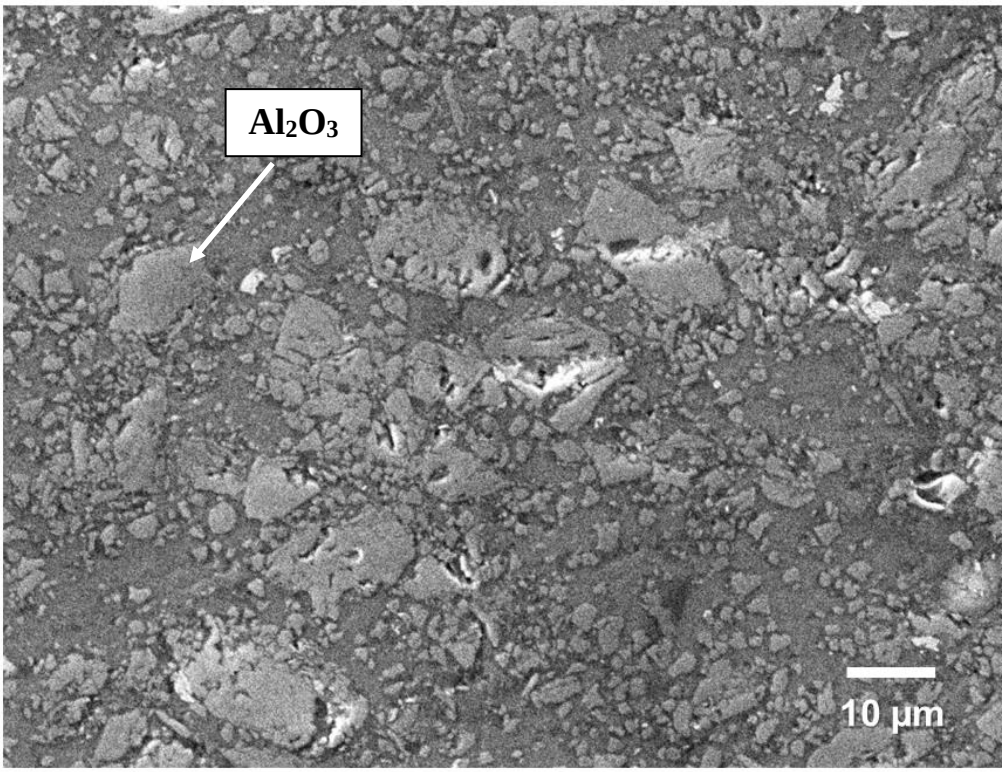

(b)

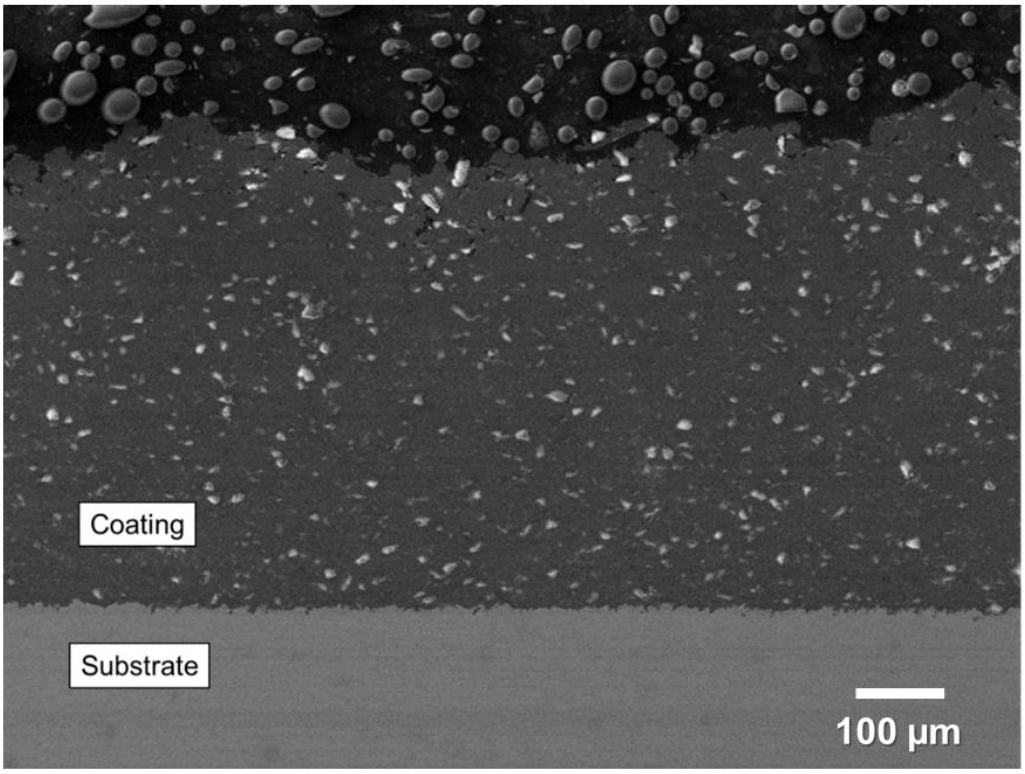

(c)

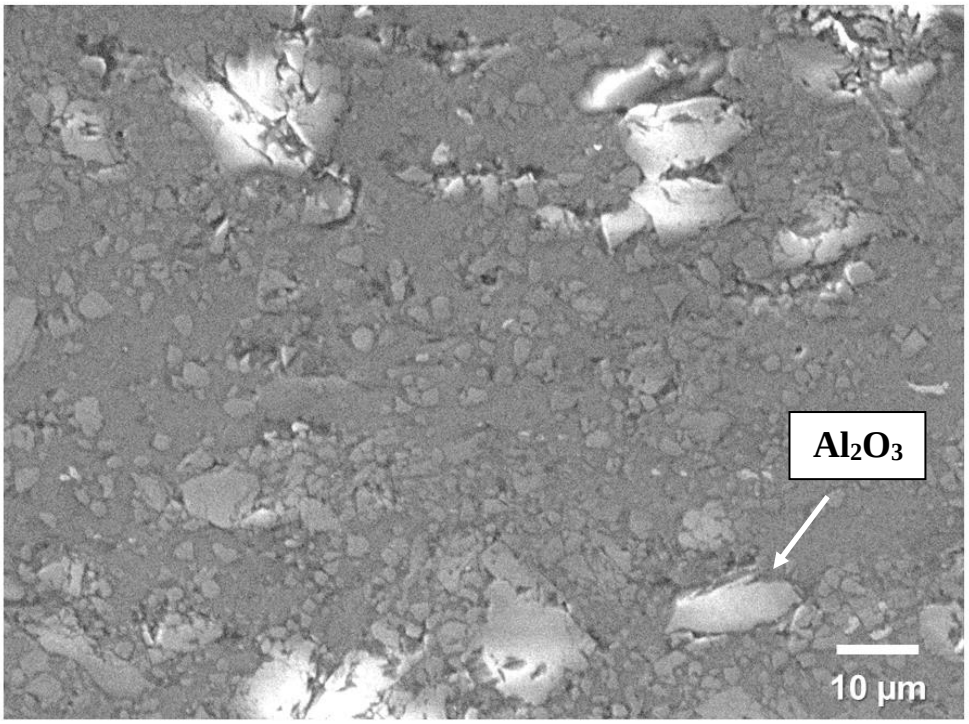

(d)

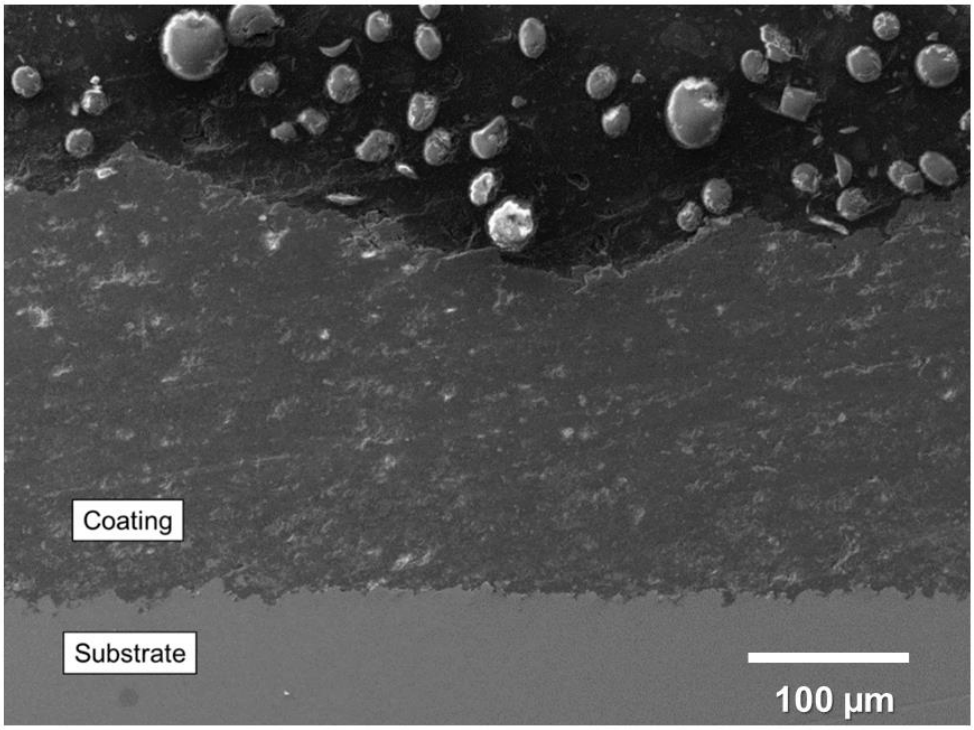

(e)

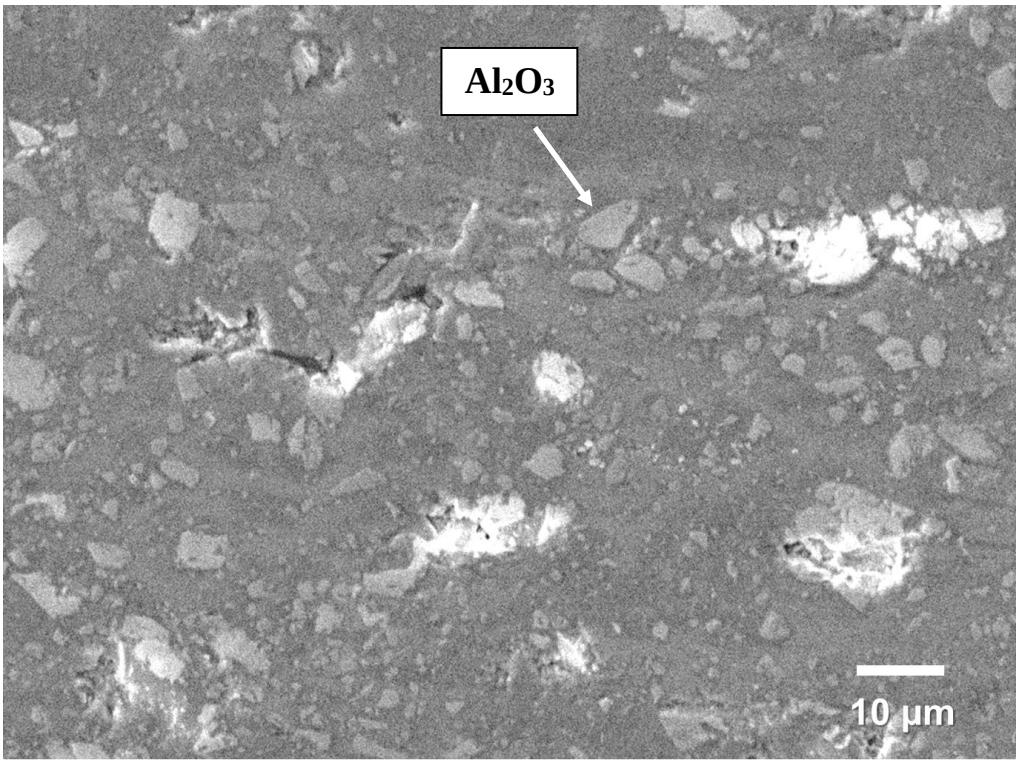

(f)

Fig. 3. **S**EM images of the Al-Al_2O_3 coatings on carbon steel: (a) 5T4 cross section; (b) 5T4 top layer of the cross section; (c) 15T4 cross section; (d) 15T4 top layer of the cross section; (e) 15T3 cross section; (f) 15T3 top layer of the cross section.

The thickness of the coatings (Table 2) was in the following order: 5T4 > 15T4 > 15T3. The thickness of the 5T4 coating was 100 µm greater than that of the 15T4 coating. When the SoD distance is increased, the free gas jet shows a continual reduction in velocity away from the nozzle, as a result of shockwaves, viscous effects, and ambient mixing, so the gas velocity at impingement decreases [17,18]. Therefore, as the SoD increased, the negative influence of the slowing nitrogen jet became stronger and the entrained aluminum particles began to decelerate, so there was a gradual reduction in particle velocity outside of the nozzle.

The gas temperature had a major effect on the coating thickness (Table 2), with the 15T4 coating being 300 µm thicker than the 15T3 coating. Particles at higher temperature are in a softer state, so less kinetic energy is required for their plastic deformation [19].

Furthermore, increase of the temperature significantly enhances bonding between the particles, increasing the thickness and cohesion strength, while decreasing the porosity [19]. These effects are beneficial in terms of obtaining a less porous coating and, consequently, improved corrosion performance [20]. In the hardness tests, the values obtained were very similar for all the coatings studied (Table 2) and were almost the same as the Al-10%Al_2O_3 coating hardness reported by Irissou et al. [21].

Table 2. Coating hardness and thickness values.

Sample	Thickness (μm)	Hardness ($HV_{0.1}$)
5T4	633 ± 11	55 ± 5
15T4	546 ± 12	55 ± 4
15T3	231 ± 9	53± 7

3.3 Corrosion results

3.3.1. Open circuit potential results

The substrate and coatings were evaluated using E_{OCP} measurements (Fig. 4) during relatively long immersion times of 120 h (steel substrate) and ~1300 h (Al-Al_2O_3 coatings). The E_{OCP} values for the substrate decreased from -0.70 V *vs.* Ag|AgCl|$KCl_{3mol/L}$ to -0.73 V *vs.* Ag|AgCl|$KCl_{3mol/L}$ after 50 h of immersion, followed by a slight increase to -0.72 V *vs.* Ag|AgCl|$KCl_{3mol/L}$ and then a slight decrease to -0.73 V *vs.* Ag|AgCl|$KCl_{3mol/L}$ until the end of the test (~200 h). The initial decrease of E_{OCP} was associated with dissolution of some of the native oxide film formed on the steel surface, as well as the adsorption of Cl^- ions on the electrode [10].

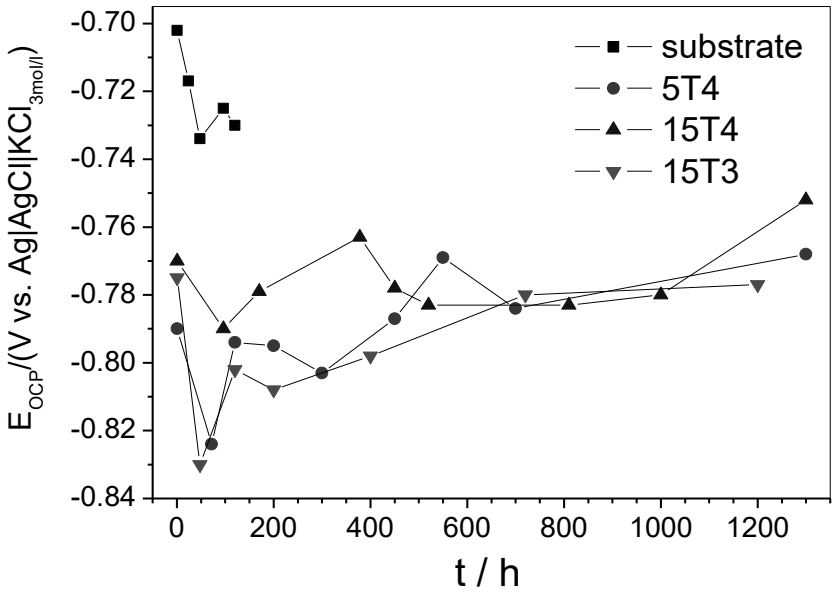

Fig. 4. Plots of open circuit potential (OCP) *vs.* time for all the samples studied. The measurements were made in aerated and unstirred 3.5 wt.% NaCl solution during relatively long immersion times, at 25 °C.

In the case of the coatings, the E_{OCP} values at initial immersion were close to -0.78 V *vs.* Ag|AgCl|$KCl_{3mol/L}$. The potentials varied up and down during the first 200 h, after which the values were similar and showed increasing trends. This similar behavior among the coatings revealed that there were no significant changes in the chemical composition of the coating/solution interface. For the 5T4 and 15T3 coatings, E_{OCP} decreased to ~-0.82 V *vs.* Ag|AgCl|$KCl_{3mol/L}$ after 50 h, followed by fluctuations up to 600 h. At the end of the experiments, E_{OCP} was ~-0.78 V *vs.* Ag|AgCl|$KCl_{3mol/L}$. For the 15T4 coating, E_{OCP} slightly decreased to -0.79 V *vs.* Ag|AgCl|$KCl_{3mol/L}$ at 50 h, then increased to -0.76 V *vs.* Ag|AgCl|$KCl_{3mol/L}$ at 400 h, and stabilized at -0.78 V *vs.* Ag|AgCl|$KCl_{3mol/L}$ at 1300 h. The decrease of E_{OCP} could be attributed to the dissolution of aluminum oxide previously formed on the surface, together with the adsorption of Cl^- ions on the electrode surface [10]. More specifically, the oscillations of potential were caused by the formation of metastable

pits/repassivation on the aluminum surface, diffusion of electrolyte through the pores of the top layer, and adsorption of Cl^- ions and a different concentration of oxygen in the bottom of the pores [10,22]. Pit initiation occurred on the defected aluminum oxide and/or in the Al metal matrix of thinner film, mainly surrounding the Al_2O_3 particles (Fig. 5). Corrosion around these particles was due to the formation of local cells between the Al matrix (more active) and the Al_2O_3 particles (more noble) [10,23]. The dissolution of aluminum occurred due to the reaction with chloride ions, with the pores becoming enlarged and some areas at the top of the coatings being damaged (Figs. 5b, 6c, 7c, and 8c). SEM images acquired at high magnification (Figs. 6a, 7a, and 8a) clearly showed that the outer layer of the coating possessed pores and/or pits. The Al_2O_3 particles were practically inert in the neutral chloride-containing solution, with the addition of alumina decreasing the active region of the electrode attacked by the electrolyte. After the E_{OCP} test, the SEM cross-sectional images showed no corrosion of the bottom layer of the coating or the substrate, probably due to the dense and almost inert nature of the coating (Figs. 6-8). Some spots of corrosion and oxides were present near the top surface (Figs. 6a, 7a, and 8a). EDS analysis (Fig. S2, *SD*) of the corroded cross section revealed the presence of aluminum and oxygen. Iron was not detected, indicating that the electrolyte had not reached the substrate, even after ~1300 h of immersion.

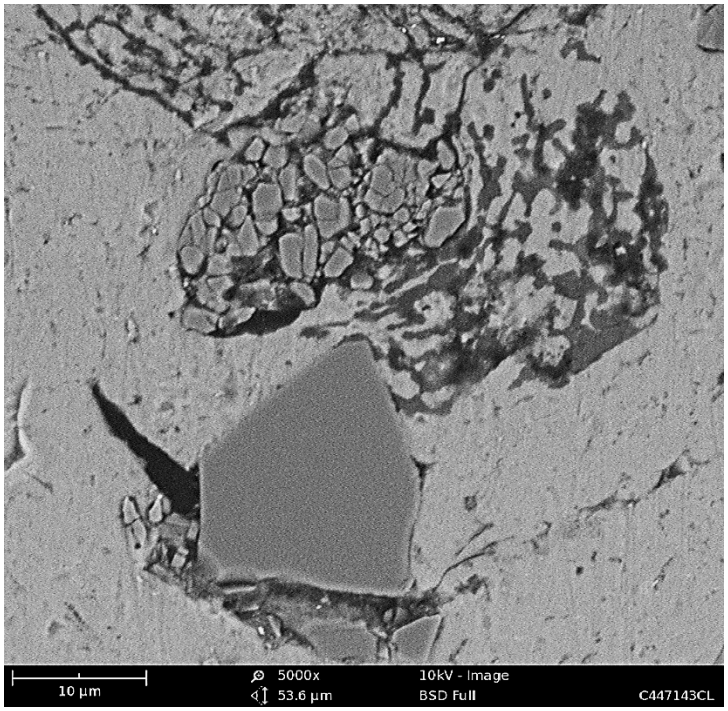

(a)

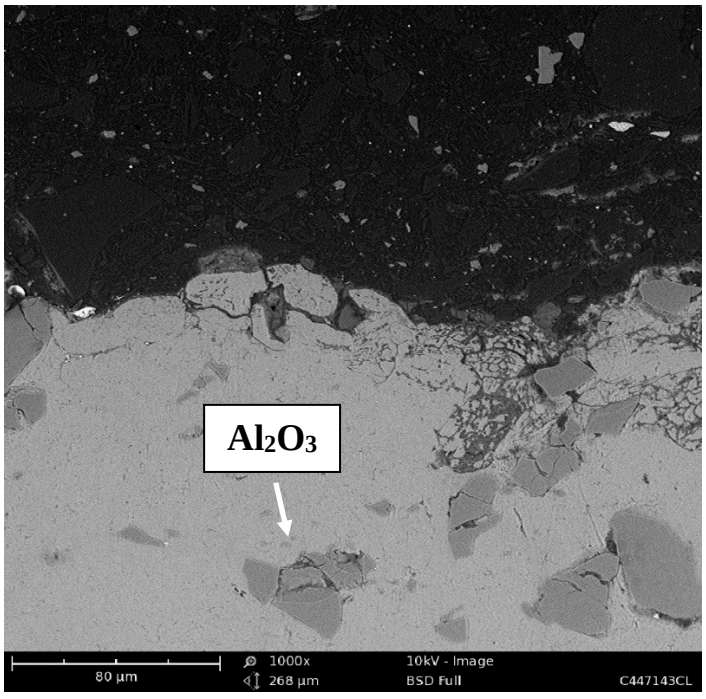

(b)

Fig. 5. SEM images of the Al-Al_2O_3 coating at magnifications of 5000x (a) and 1000x (b), after long immersion (t ~1300 h), during which the E_{OCP} and EIS measurements were performed. The images show defects and dissolution of the Al matrix surrounding the alumina particles.

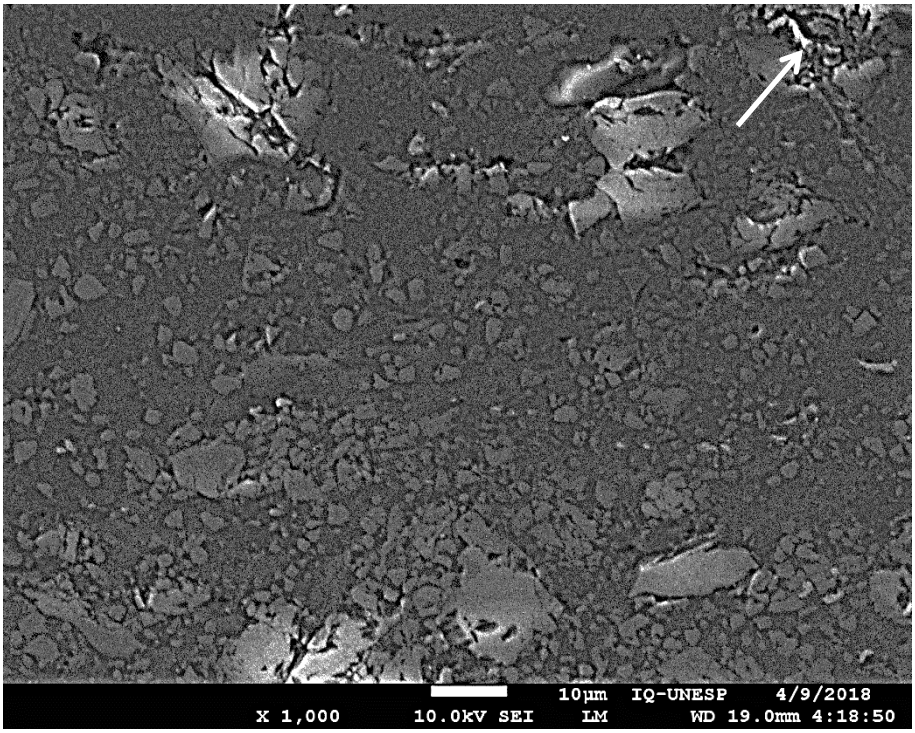
10µm IQ-UNESP 4/9/2018
X 1,000 10.0kV SEI LM WD 19.0mm 4:18:50

(a)

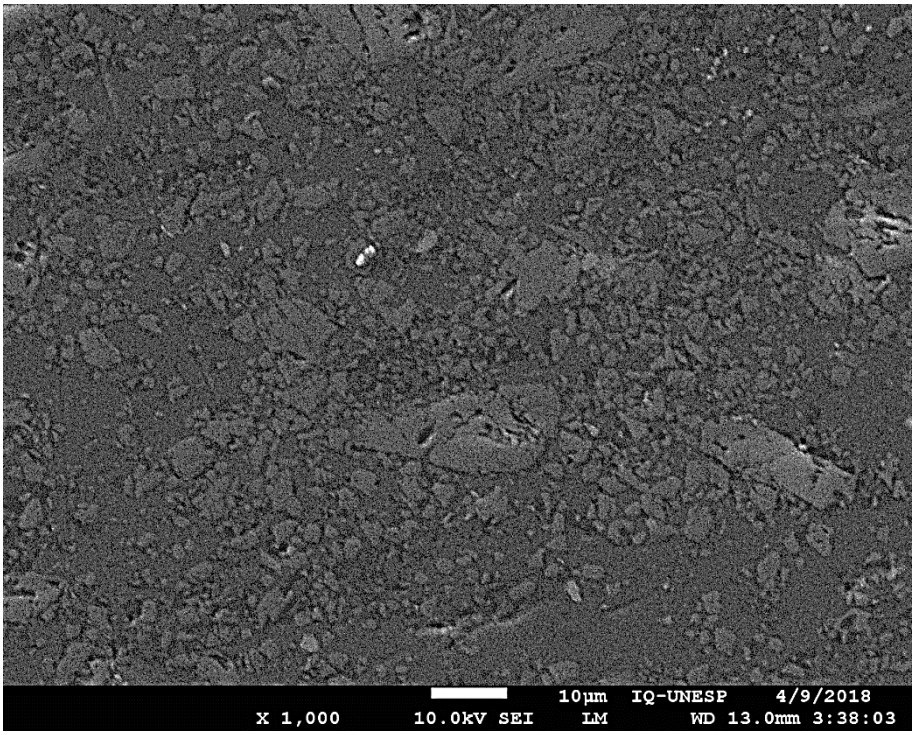
10µm IQ-UNESP 4/9/2018
X 1,000 10.0kV SEI LM WD 13.0mm 3:38:03

(b)

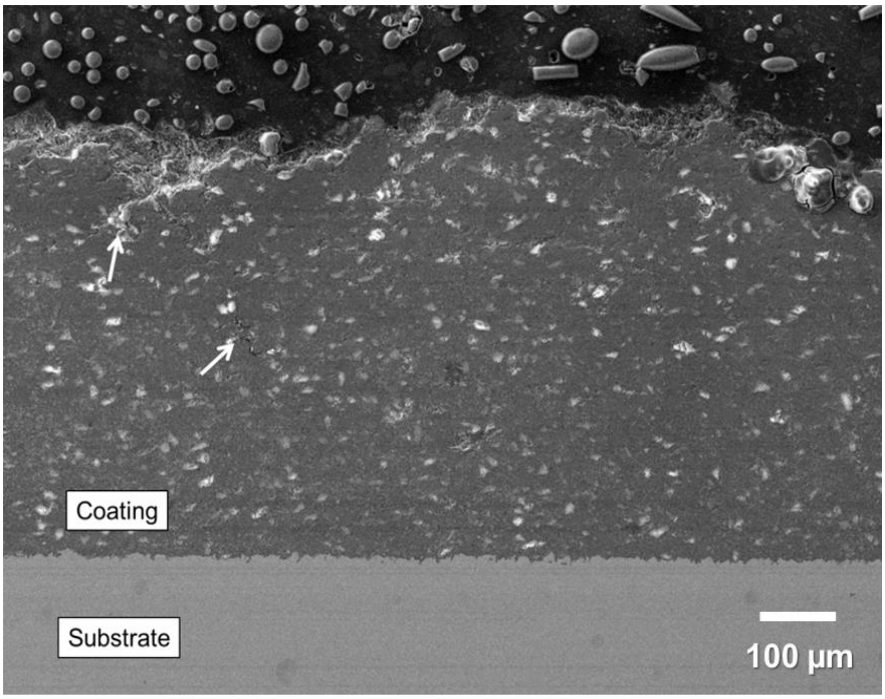

(c)

Fig. 6. SEM images of sample 5T4 after 1200 h of immersion in 3.5 wt.% NaCl solution, showing (a) the upper region of the coating, (b) the bottom region of the coating, and (c) the cross section of the coating. The arrows indicate defects and pores.

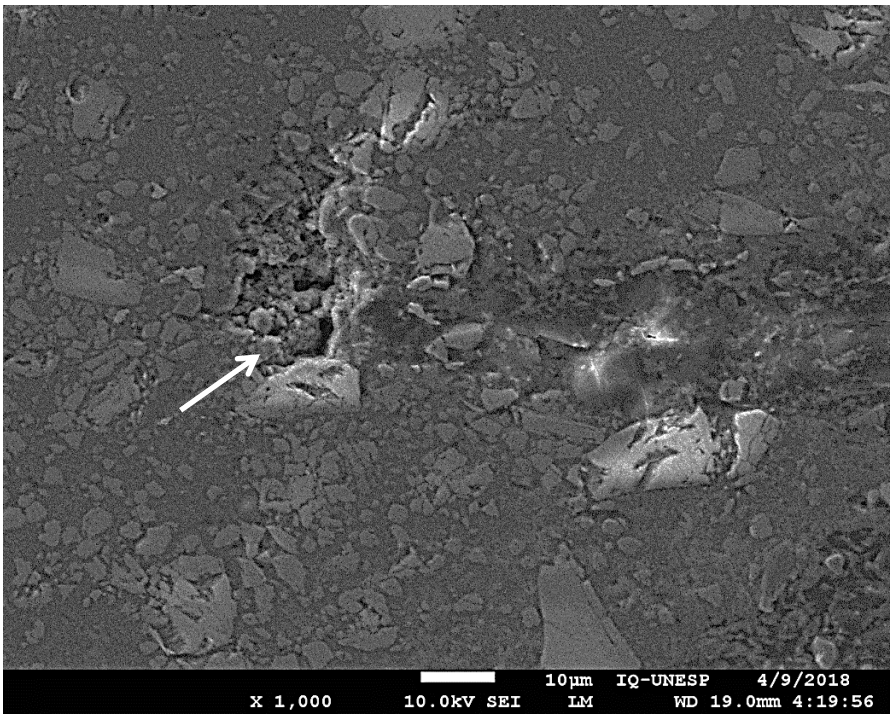

(a)

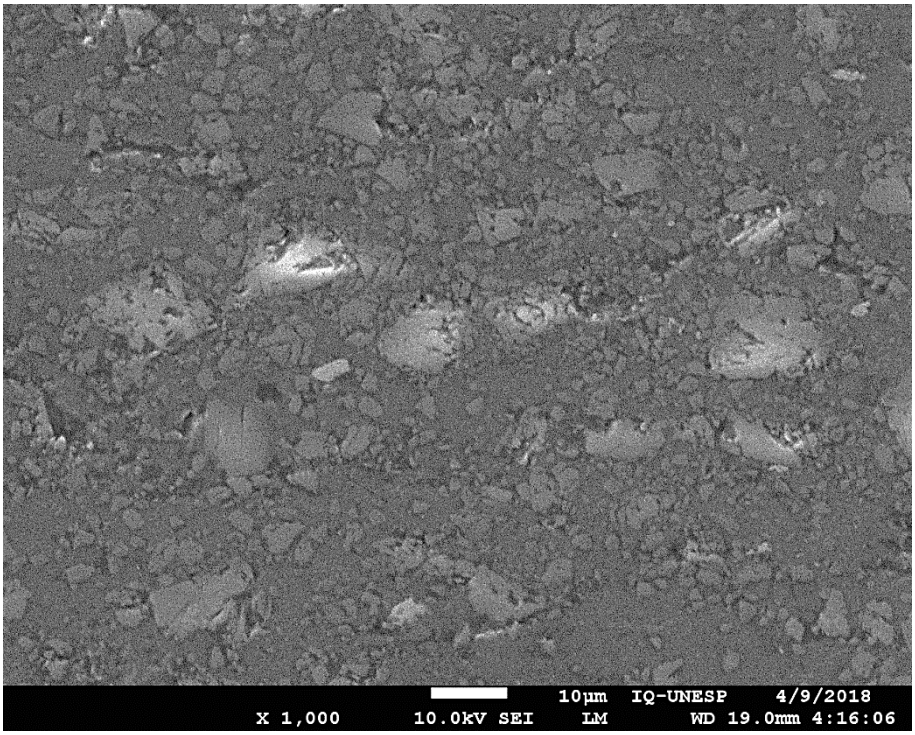

(b)

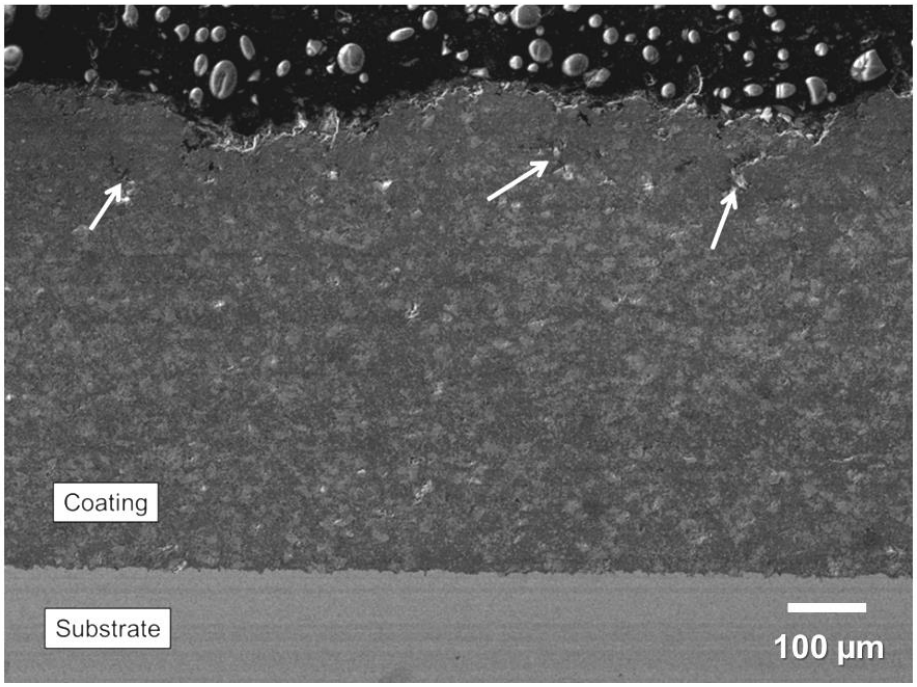

(c)

Fig. 7. SEM images of sample 15T4 after 1200 h of immersion in 3.5 wt.% NaCl solution, showing (a) the upper region of the coating, (b) the bottom region of the coating, and (c) the cross section of the coating. The arrows indicate defects and pores.

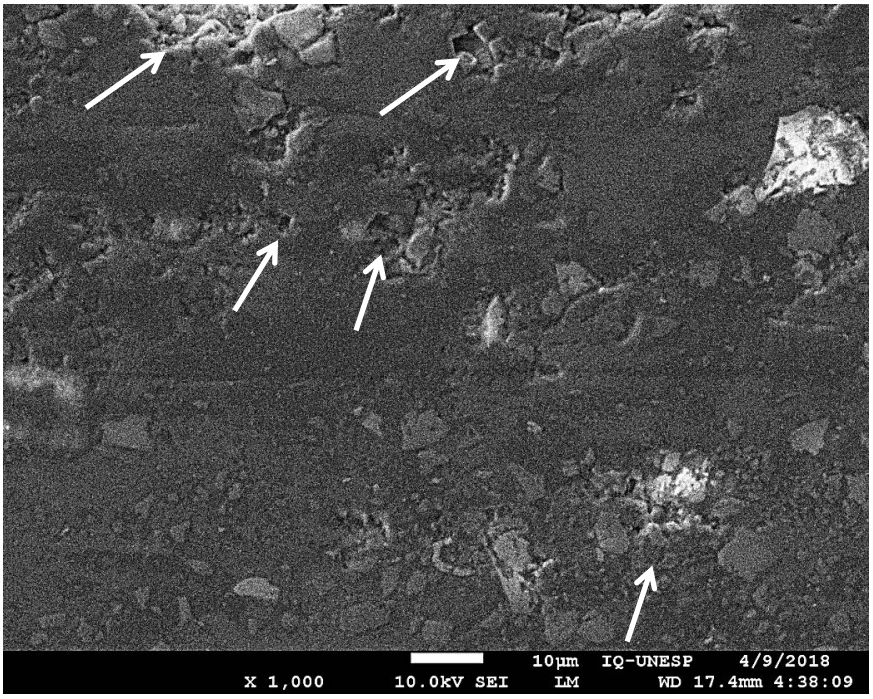
10µm IQ-UNESP 4/9/2018
X 1,000 10.0kV SEI LM WD 17.4mm 4:38:09

(a)

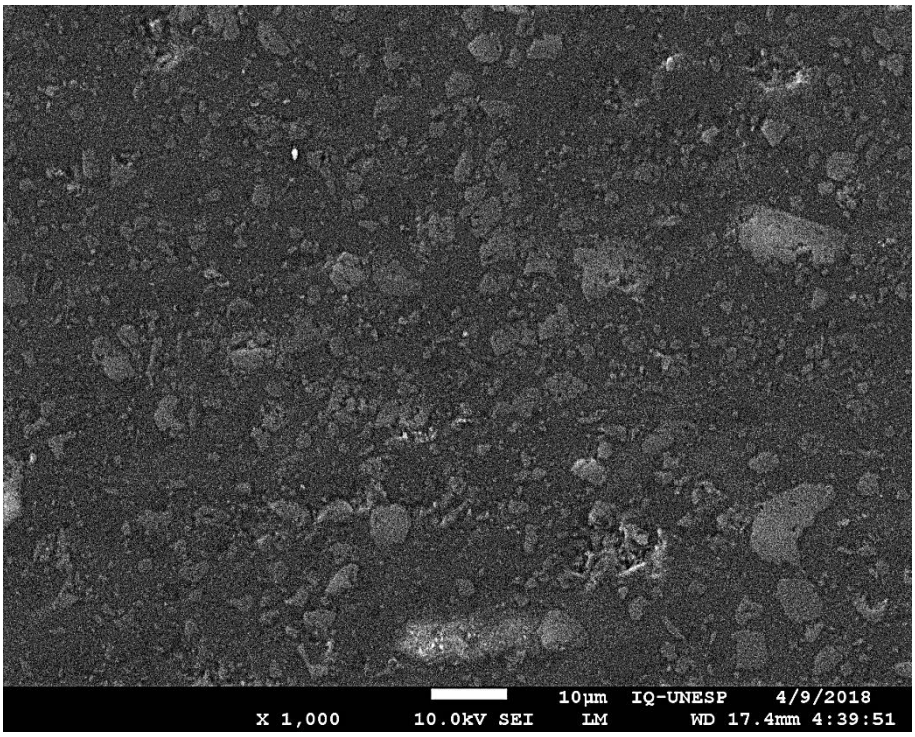
10µm IQ-UNESP 4/9/2018
X 1,000 10.0kV SEI LM WD 17.4mm 4:39:51

(b)

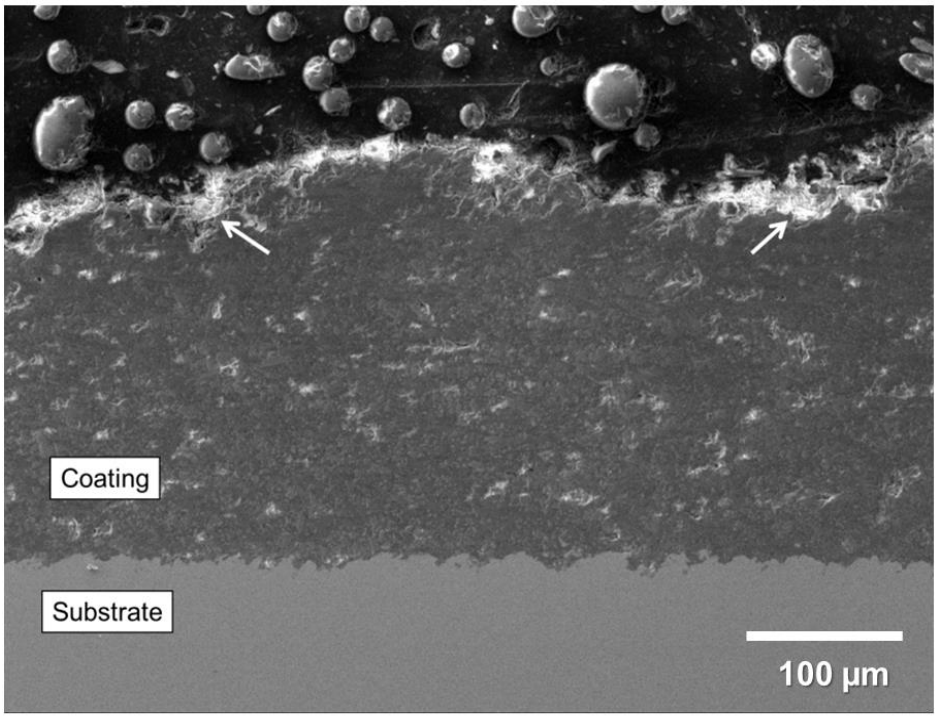

(c)

Fig. 8. SEM images of sample 15T3 after 1200 h of immersion in 3.5 wt.% NaCl solution, showing (a) the upper region of the coating, (b) the bottom region of the coating, and (c) the cross section of the coating. The arrows indicate defects and pores.

3.3.1. EIS results

Fig. S3 (*SD*) shows the EIS diagrams for the steel substrate, as a function of immersion time. Figs. S4 and S5 (*SD*) show representative impedance diagrams for the Al-Al_2O_3 coatings. Impedance results for each coating (>5 diagrams per coating) were recorded throughout the duration of the experiment. The results obtained at ~200 h and ~1300 h are presented as being representative of the set of experiments.

For the steel substrate, the EIS results showed a semicircle in the Nyquist diagram (Fig. S3, *SD*), while the Bode phase angle diagrams showed an asymmetric time constant in the medium frequency (MF) range (Fig. S3, *SD*), suggesting the existence of two time constants. The semicircle of the complex plane decreased between 48 h and 120 h, indicative

of dissolution of the oxide layer and/or desorption of ions. Accordingly, the impedance modulus values also decreased in the low frequency (LF) range, which could be attributed to iron oxidation and dissolution of the porous iron oxides film.

At immersion times of ~200 h and ~1300 h (Figs. S4 and S5, *SD*), the Nyquist plots for the coatings showed the presence of two separated semicircles. The amplitudes of the semicircles were greater for the 15T3 coating. Accordingly, the 15T3 sample showed the highest |Z| value. The Bode phase plots at medium to high frequencies (MF-HF) showed an asymmetric time constant, indicating the presence of two overlapped time constants. The difference between the diagrams was a slightly higher phase angle for the 15T3 coating. As reported previously for CGS Al-Al_2O_3 coatings [10,24], the time constant at medium to high frequency is composed by two partially overlapped time constants, one attributed to the alumina itself (formed at the Al surface) and the other to aluminum oxidation (Al to Al^+, and Al^+ to Al^{3+}) at the coating/solution interface. The time constant at f <0.1 Hz was assigned to dissolution of the aluminum oxide and diffusion of ions through a deteriorated barrier layer [10].

The experimental EIS data obtained for the steel substrate and the coatings, at different immersion times, were quantitatively analyzed using the electrical equivalent circuit (EEC) shown in Fig. 9. The suitability of this EEC was supported by the chi-squared (χ^2) values of around 10^{-4}, with errors <10% for each parameter (Table S1, *SD*), as well as by good agreement between the fitted and experimental impedance diagrams (Figs. S6-S9, *SD*), as found previously [10]. In this scheme, where R_s is the uncompensated solution resistance, the time constant in the MF region is described by the sub-circuit $CPE_{dl}//R_{ct}$, attributed to oxygen reduction and iron oxidation. CPE_{dl} is the constant phase element composed by the admittance CPE_{dl}-*T*, which is proportional to the capacitance of the electrical double layer and the exponent CPE_{dl}-*P* (n_{dl}), and R_{ct} is the charge transfer resistance. The data for the LF

region are described by the CPE_{film}/R_{film} sub-circuit, which is related to formation/dissolution of the non-protective film and desorption of iron ions. The element CPE_{film} is the constant phase element associated as described previously, with CPE_{film}-T being proportional to the capacitance of the film (adsorbed species and iron oxides-hydroxides) and the exponent n_{film}. The element R_{film} is the resistance of the film and the electrolyte inside the defects and pores of the film [10]. For the coatings, the $CPE_{dl}//R_{ct}$ sub-circuit has the same meaning described previously. R_{ct} is associated with the anodic and cathodic processes involving oxidation of the Al matrix and the reduction of oxygen from the solution on the Al_2O_3 particles. The $CPE_{film}//R_{film}$ sub-circuit represents the constant phase element (CPE_{film}) of the aluminum oxide in parallel with the resistance (R_{film}) that comprises the resistance of the oxide film/products of corrosion and the resistance of the solution inside the pores.

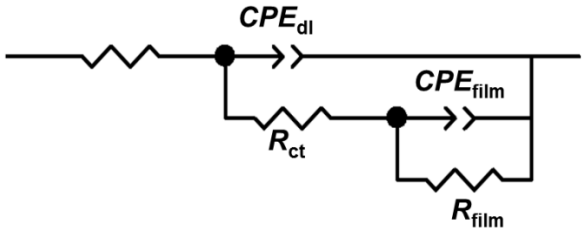

Fig. 9. Electrical equivalent circuit used to fit the EIS data for the steel substrate and the Al-Al_2O_3 coatings.

The changes of R_{ct} and R_{film} for the coatings, according to immersion time, are shown in Fig. 10. For the 5T4 and 15T4 coatings, R_{ct} increased almost continuously during the immersion, from around 2 kΩ cm^2 to 5.3 kΩ cm^2 and 8.5 kΩ cm^2 for the 5T4 and 15T4 coatings, respectively. This increase was associated with the formation of corrosion products, mainly aluminum oxide on the active Al regions, which limited the coating corrosion to the top layer [10]. The difference between the R_{ct} values for these two coatings was probably

related to the microstructure of the protective oxide layer, which allowed the electrolyte to reach greater areas of Al in the case of 5T4, compared to 15T4. For the 15T3 coating, R_{ct} of ~9 kΩ cm^2 was obtained at initial immersion, followed by an increase to ~15 kΩ cm^2 and then a continuous decrease to 2 kΩ cm^2 after 600 h of immersion. The increase of R_{ct} occurred for the same reason described above, namely the formation of an oxide layer. As observed previously (Figs. 3e, 3f, and 8), the microstructure of the 15T3 coating was more porous and presented more cracks and defects, leading to the formation of a defective aluminum oxide layer that was easily attacked. These defects allowed access of the electrolyte solution to a greater area of the coating, mainly around the alumina particles, forming local cells and consequently initiating corrosion of the Al matrix, as observed in the SEM images (Fig. 8). These local cells accelerated the dissolution of aluminum, which was responsible for the decrease of R_{ct} after 600 h.

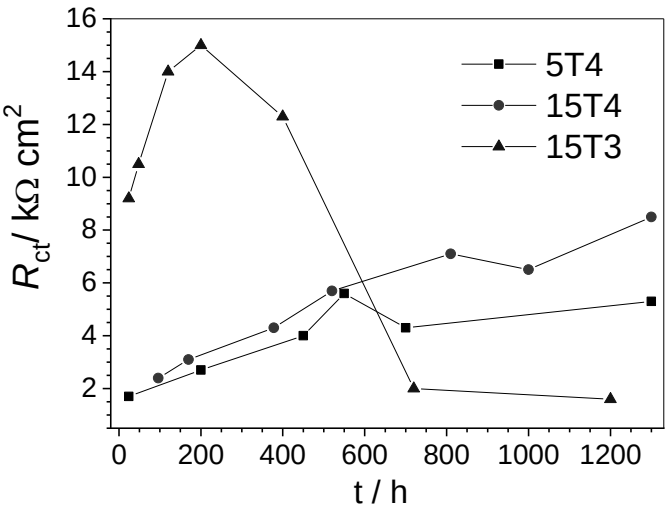

(a)

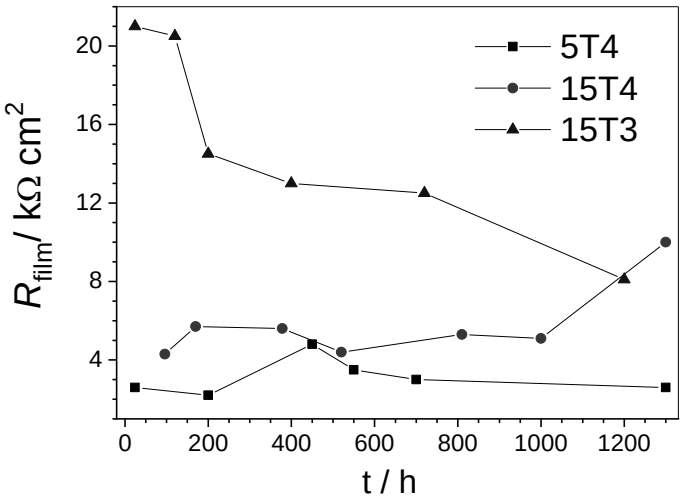

(b)

Fig. 10. (a) R_{ct} and (b) R_{film} for the Al-Al_2O_3 coatings in 3.5 wt.% NaCl solution at 25 °C.

For sample 5T4, the increase of R_{film} between 1 h and ~400 h could be attributed to the increase of the film thickness, while the decrease at t >400 h could be explained by increase of the film porosity. For sample 15T3, R_{film} decreased rapidly from 21 to 15 kΩ cm^2 during the first 200 h of immersion, followed by a continuous decrease to 8 kΩ cm^2 up to 1200 h. The decrease of R_{film} could be attributed to increased porosity of the film and chloride attack on the coating, leading to film dissolution [10]. For the 15T4 coating, R_{film} remained almost constant at around 6 kΩ cm^2 during the first 1000 h of the test, followed by an increase to 10 kΩ cm^2 at 1300 h of immersion, suggesting that there was progressive formation of a more compact oxide layer.

The electrochemical impedance results indicated that sample 15T4 showed the best performance, while the coating/substrate interface of all the coatings remained intact and did not undergo any damage during the entire duration of immersion in the chloride solution.

4. Conclusions

The results showed that the spray temperature and standoff distance influenced the coating thickness, microstructure, and corrosion resistance. Increase of the standoff distance slightly decreased the coating thickness, while a 100 °C decrease of the spraying temperature reduced the coating thickness by more than 300 µm. The thickness values of the coatings were in the following order: 5T4 > 15T4 > 15T3. The 15T3 coating showed the lowest thickness (231 µm) and presented a microstructure with a greater quantity of cracks and defects. The 5T4 sample showed the highest thickness (633 µm) and a dense microstructure. However, due to the tamping effect, all the coatings functioned as dense barriers without interconnected porosity, enabling them to protect the substrate, even after 1200 h of immersion.

5. Acknowledgements

The authors thank CNPq (Conselho Nacional de Pesquisa, grants 153177/2014-4 and 201325/2014-4) and PNPD/CAPES (Coordenação de Aperfeiçoamento de Pessoal de Nível Superior) for financial support and scholarships.

6. References

[1] A. Vardelle, C. Moreau, J. Akedo, H. Ashrafizadeh, C.C. Berndt, J.O. Berghaus, M. Boulos, J. Brogan, A.C. Bourtsalas, A. Dolatabadi, M. Dorfman, T.J. Eden, P. Fauchais, G. Fisher, F. Gaertner, M. Gindrat, R. Henne, M. Hyland, E. Irissou, E.H. Jordan, K.A. Khor, A. Killinger, Y.C. Lau, C.J. Li, L. Li, J. Longtin, N. Markocsan, P.J. Masset, J. Matejicek, G. Mauer, et al., The 2016 Thermal Spray Roadmap, J. Therm. Spray Technol. 2016; 25(8): 1376–1440.

[2] W. Li, K. Yang, S. Yin, X. Yang, Y. Xu, and R. Lupoi, Solid-State Additive

Manufacturing and Repairing by Cold Spraying: A Review, J. Mater. Sci. Technol. 2018; 34(3): 440–457.

[3] Y. Tao, T. Xiong, C. Sun, H. Jin, H. Du, and T. Li, Effect of α-Al2O3 on the Properties of Cold Sprayed Al/α-Al2O3 Composite Coatings on AZ91D Magnesium Alloy, Appl. Surf. Sci. 2009; 256(1): 261–266.

[4] K. Spencer, D.M. Fabijanic, and M.X. Zhang, The Use of Al-Al2O3 Cold Spray Coatings to Improve the Surface Properties of Magnesium Alloys, Surf. Coatings Technol. 2009; 204(3): 336–344.

[5] R. Fernandez and B. Jodoin, Cold Spray Aluminum–Alumina Cermet Coatings: Effect of Alumina Content, J. Therm. Spray Technol. 2018; 27(4): 603–623.

[6] D. Cong, Z. Li, Q. He, H. Chen, Z. Zhao, L. Zhang, and H. Wu, Wear Behavior of Corroded Al-Al_2O_3 Composite Coatings Prepared by Cold Spray, Surf. Coatings Technol. 2017; 326: 247–254.

[7] X. Qiu, N. ul H. Tariq, J. Wang, J. Tang, L. Gyansah, Z. Zhao, and T. Xiong, Microstructure, Microhardness and Tribological Behavior of Al2O3 Reinforced A380 Aluminum Alloy Composite Coatings Prepared by Cold Spray Technique, Surf. Coatings Technol. 2018; 350: 391–400.

[8] V.K. Champagne, The Cold Spray Materials Deposition Process: Fundamentals and Applications, 2007.

[9] C. Zhao, H. Zhang, T. Shao, and C. Dou, Microstructure and Corrosion Behaviour of Al Coating Deposited by Cold Spraying onto FSW AA2219-T87 Joint, Corros. Eng. Sci. Techn. 2019; 54(1): 86–92.

[10] F.S. d. Silva, J. Bedoya, S. Dosta, N. Cinca, I.G. Cano, J.M. Guilemany, and A. V. Benedetti, Corrosion Characteristics of Cold Gas Spray Coatings of Reinforced Aluminum Deposited onto Carbon Steel, Corros. Sci. 2017; 114: 57–71.

[11] W.S. Tait, An Introduction to Electrochemical Corrosion Testing for Practicing Engineers and Scientists, Wisconsin Pair Odocs, 1994.

[12] M. Orazem and B. Tribollet, Electrochemical Impedance Spectroscopy, 1st ed., John Wiley & Sons, New Jersey, 2008.

[13] X. Zhou and P. Mohanty, Electrochemical Behavior of Cold Sprayed Hydroxyapatite/Titanium Composite in Hanks' Solution, Electrochim. Acta 2012; 65: 134–140.

[14] R.B. Heimann, J.I. Kleiman, S. Marx, R. Ng, S. Petrov, M. Shagalov, R.N.S. Sodhi, and A. Tang, High-Pressure Cold Gas Dynamic (CGD) - Sprayed Alumina-Reinforced Aluminum Coatings for Potential Application as Space Construction Material, Surf. Coat. Technol. 2014; 252: 113–119.

[15] Y. Tao, T. Xiong, C. Sun, H. Jin, H. Du, and T. Li, Effect of α-Al_2O_3 on the Properties of Cold Sprayed Al/α-Al_2O_3 Composite Coatings on AZ91D Magnesium Alloy, Appl. Surf. Sci. 2009; 256(1): 261–266.

[16] S. Yin, P. Cavaliere, B. Aldwell, R. Jenkins, H. Liao, W. Li, and R. Lupoi, Cold Spray Additive Manufacturing and Repair: Fundamentals and Applications, Addit. Manuf. 2018; 21; 628–650.

[17] J. Pattison, S. Celotto, A. Khan, and W. O'Neill, Standoff Distance and Bow Shock Phenomena in the Cold Spray Process, Surf. Coatings Technol. 2008; 202(8): 1443–1454.

[18] T. Stoltenhoff, H. Kreye, and H.J. Richter, An Analysis of the Cold Spray Process and Its Coatings, J. Therm. Spray Technol. 2002; 11(4): 542–550.

[19] X. Meng, J. Zhang, J. Zhao, Y. Liang, and Y. Zhang, Influence of Gas Temperature on Microstructure and Properties of Cold Spray 304SS Coating, J. Mater. Sci. Technol. 2011; 27(9): 809–815.

[20] S.M. Hassani-Gangaraj, A. Moridi, and M. Guagliano, Critical Review of Corrosion Protection by Cold Spray Coatings, Surf. Eng. 2015; 31(11): 803–815.

[21] E. Irissou, J.G. Legoux, B. Arsenault, and C. Moreau, Investigation of Al-Al_2O_3 Cold Spray Coating Formation and Properties, J. Therm. Spray Technol. 2007; 16(5–6): 661–668.

[22] E. McCafferty, Sequence of Steps in the Pitting of Aluminum by Chloride Ions, Corros. Sci. 2003; 45(7): 1421–1438.

[23] N. Birbilis and R.G. Buchheit, Electrochemical Characteristics of Intermetallic Phases in Aluminum Alloys, J. Electrochem. Soc. 2005; 152(4): B140–B151.

[24] S.E. Frers, M.M. Stefenel, C. Mayer, and T. Chierchie, AC-Impedance Measurements on Aluminium in Chloride Containing Solutions and below the Pitting Potential, J. Appl. Electrochem. 1990; 20(6): 996–999.